Li-Rich Mn–Mg Layered Oxide as a Novel Ni-/Co-Free Cathode

Yongseok Lee, Hyunyoung Park, Min-kyung Cho, Jinho Ahn, Wonseok Ko, Jungmin Kang, Yoo Jung Choi, Hyungsub Kim, Inchul Park, Won-Hee Ryu, Jihyun Hong,* and Jongsoon Kim*

Although Li_2MnO_3 exhibits high capacity via anionic oxygen redox, it suffers from rapid capacity decay owing to structural disordering accompanying irreversible Mn migration and O_2 release. To promote the reversibility of the anionic redox reaction, $Li_{1.8}Mg_{0.3}Mn_{0.9}O_3$ as a novel cathode material, prepared by partially substituting Li^+ and Mn^{4+} of Li_2MnO_3 with the redox-inactive Mg^{2+} as a structural stabilizer is proposed. $Li_{1.8}Mg_{0.3}Mn_{0.9}O_3$ delivers a high specific capacity and energy density of ≈ 310 mAh g^{-1} and ≈ 915 Wh kg^{-1}, respectively. In particular, the power-capability and cycle performance of $Li_{1.8}Mg_{0.3}Mn_{0.9}O_3$ greatly surpass those of Li_2MnO_3. Through first-principles calculations and various experiments, it is revealed that Mg substitution effectively suppresses the Mn migration by stabilizing Mn cations in the original sites at the charged state. The energetically stabilized layered structure disfavors the distortion of the MnO_6 octahedra, which induces the oxygen dimer (O—O) formation through the metal–oxygen deco-ordination, thus mitigating oxygen release.

1. Introduction

Recently, lithium-ion batteries (LIBs) have received great attention as energy storage systems (ESSs) with outstanding efficiency and have thus been employed in a wide range of applications from small electronic devices to grid-scale ESSs.[1–3] Among various cathode materials for LIBs, Ni-Co-based layered oxides, such as $LiNi_xCo_yMn_zO_2$ (NCM) or $LiNi_xCo_yAl_zO_2$ (NCA), are regarded as promising cathode materials because of their high operation voltage and theoretical capacity, which lead to superior energy densities.[4,5] However, the explosive demand for raw materials has resulted in a rapid surge in prices, hindering the development of industries requiring high-capacity energy storage devices. In particular, Ni and Co are not favorable metal resources given the drastic price surge over the past few years. In 2019, the prices of Co and Ni were 30 000 and 12 000 USD/ton; however, in 2022, these prices have soared to 81 880 and 42 995 USD/ton, respectively.[6] Unsurprisingly, in electric vehicle markets around the globe, materials such as $LiFePO_4$ (LFP) or Mn-rich compounds are being selected as cathode materials for LIBs rather than expensive NCM or NCA (Fe: 142 USD/ton, Mn: 1735 USD/ton in 2022).

Li-rich layered oxides $(Li_{1+x}(TM)_{1-x}O_2)$ with large theoretical capacities are promising cathodes for next-generation LIBs.[7–14] Because the Li ions occupy both the Li and transition metal (TM) layers possessing in-plane ordering Li/Mn ions, Li-/Mn-rich layered oxides can deliver large available Li^+ contents and theoretical capacities during charge/discharge compared with the conventional layered oxides, $Li(TM)O_2$.[15] In particular, Ni-/Co-free Li_2MnO_3 possesses great merits as an outstanding cathode material, such as a large theoretical capacity of 456 mAh g^{-1} corresponding to 2 mol Li^+ de/intercalation and a low production

Y. Lee, H. Park, J. Ahn, W. Ko, J. Kang, J. Kim
Department of Energy Science
Sungkyunkwan University
Suwon 16419, Republic of Korea
E-mail: jongsoonkim@skku.edu

Y. Lee, H. Park, J. Ahn, W. Ko, J. Kang, J. Kim
SKKU Institute of Energy Science and Technology (SIEST)
Sungkyunkwan University
Suwon 16419, Republic of Korea

M.-k. Cho
Advanced Analysis Center
Korea Institute of Science and Technology (KIST)
Seoul 02792, Republic of Korea

Y. J. Choi, W.-H. Ryu
Department of Chemical and Biological Engineering
Sookmyung Women's University
Seoul 04310, Republic of Korea

H. Kim
Korea Atomic Energy Research Institute (KAERI)
Daejeon 34057, Republic of Korea

I. Park
Battery Materials Research Center
Research Institute of Industrial Science and Technology (RIST)
Incheon 21985, Republic of Korea

J. Hong
Energy Materials Research Center
Korea Institute of Science and Technology (KIST)
Seoul 02792, Republic of Korea
E-mail: jihyunh@kist.re.kr

ADVANCED
SCIENCE NEWS
www.advancedsciencenews.com

ADVANCED
FUNCTIONAL
MATERIALS
www.afm-journal.de

cost through the use of earth-abundant Mn. Although Li_2MnO_3 was considered to be electrochemically inactive in early studies because of the difficulty of achieving the cationic redox reaction between Mn^{4+} and Mn^{5+} in the octahedra coordination, recent studies have demonstrated that Li^+ in the Li_2MnO_3 structure can be deintercalated through the anionic redox reaction (O^{2-}/O^-).[7,16–18] However, Li_2MnO_3 exhibits a severe level of irreversible capacity due to structural degradation during the Li^+ de/intercalation, which is noticeable in the initial cycle.[19]

Reactions resulting in the structural degradation of Li_2MnO_3 have been reported to occur during charge/discharge, such as Mn migration to the Li layers (resulting in a Li/Mn disordered rock-salt phase) accompanying oxygen release due to the loss of oxygen molecules from the structure.[20–22] Intensive efforts have focused on mitigating the capacity fading and structural degradation of Li-rich cathode materials upon cycling.[23,24] These issues associated with Li_2MnO_3 can be easily overcome through the addition of a structural stabilizer to prevent the irreversible Mn migration. We speculated that magnesium cations (Mg^{2+}), which strongly favor octahedral sites, could effectively suppress not only the distortion of Mn octahedra of oxidized oxygen anions but also Mn migration to Li layers. Nayak et al. reported that the doped Mg^{2+} ions firmly hold oxygen, forming Mg–O bonds, which are stronger than Li–O bonds, thereby restricting the irreversible release of Li^+ and O_2 from the Li_2MnO_3 structure.[25] Wang et al. suggested that $Li[Li_{0.2}Ni_{0.195}Mn_{0.595}Mg_{0.01}]O_2$ achieved significant improvement in the rate capability and cycle performance.[26] Thus, these studies indicate that the Mg^{2+} in the structure enables the occurrence of the reversible anionic redox reaction (O^{2-}/O^-) without severe disordering.[27–29]

In this study, we propose $Li_{1.8}Mg_{0.3}Mn_{0.9}O_3$ (hereafter LMMO) as a novel Li-rich Mg–Mn layered oxide cathode, designed by partial substitution of 0.1 mol Mn^{4+} and 0.2 mol Li^+ in Li_2MnO_3 with 0.3 mol Mg^{2+}. LMMO exhibited a large specific capacity of ≈310 mAh g^{-1} at 30 mA g^{-1} and stable cycle retention of ≈72% over 200 cycles at 1 A g^{-1} with outstanding coulombic efficiency (CE), vastly superior to the electrochemical performance of pristine Li_2MnO_3 (hereafter LMO). Mg^{2+} substitution into the Li-/Mn-rich layered oxide cathode materials offered many advantages beyond improving the electrochemical performance. The reversible structure change of LMMO with anionic redox behavior during charge/discharge was investigated using various computational/experimental techniques, including first-principles calculation, high-angle annular dark-field scanning transmission electron microscopy (HAADF-STEM), ex situ/operando X-ray diffraction (XRD), X-ray absorption near edge structure (XANES) spectroscopy, extended X-ray absorption fine structure (EXAFS) spectroscopy, and soft X-ray absorption spectroscopy (sXAS).

2. Results and Discussion

2.1. Merit of $Li_{1.8}Mg_{0.3}Mn_{0.9}O_3$ (LMMO)

Figure S1 (Supporting Information) compares LMMO and conventional materials in terms of production price and capacity. LMMO is suitable for the establishment of economical and eco-friendly large-scale energy storage systems owing to the earth-abundant Mn resources as well as excellent energy density and power-capability comparable to those of other conventional cathode materials, such as $LiCoO_2$, $LiNi_{0.8}Co_{0.1}Mn_{0.1}O_2$, $LiNi_{0.8}Co_{0.1}Al_{0.1}O_2$, and $LiNi_{0.6}Co_{0.2}Mn_{0.2}O_2$.[30–33] As shown at **Figure 1**a, LMMO has a monoclinic C 1 2/m 1 structure, with a structure formula corresponding to $Li_{1.5}^{(Li)}[Li_{0.3}Mg_{0.3}Mn_{0.9}]^{(TM)}O_3$, consisting of a Li layer and a TM layer of Mn^{4+}, Mg^{2+}, and Li^+ forming honeycomb-like in-plane ordering. Similarly, LMO can be expressed as $Li_{1.5}^{(Li)}[Li_{0.5}Mn]^{(TM)}O_3$, of which the TM layer contains more Li^+ than LMMO. Despite the higher Li content, we noted that the practically available Li^+ for deintercalation from the LMO cathode is significantly limited as a result of the irreversible structural failure occurring during charge/discharge. In particular, the presence of the redox-inactive Mg^{2+} as a structural stabilizer not only suppresses the structural disordering by the Mn migration but also enables the occurrence of the reversible anionic redox reaction. The substitution of Mg^{2+} in the TM layers was expected to theoretically increase the formal oxidation states of oxygen from 1.33 in $Mn^{(4+)}O_3$ to 1.4 in $Mg_{0.3}Mn^{(4+)}_{0.9}O_3$, reducing the instability caused by excessive oxidation of oxygen.

With the aid of the structural rigidity of the MgO_6 octahedra, the redox-inactive Mg^{2+} enhanced the structural stability of the Li-rich layered oxides during electrochemical cycling.[34] The similarity between the XRD patterns of LMMO and LMO indicates the analogous layered structure of both materials (Figure S2, Supporting Information). In both XRD patterns, the superlattice peaks appear in the 2θ range of 20°–32°, originating from the honeycomb-like in-plane ordering of Li and Mn/Mg.[12,13,35] We note that the intensity ratio of the (001) to (131) peaks increased with Mg substitution, attributable to the enhanced contrast between Li layers and (Li/Mn) layers and indicating the preferred Mg^{2+} occupancy in (Li/Mn) layers. To resolve the crystal structure of LMMO, we performed Rietveld refinement of the XRD pattern (Figure 1b). The lattice parameters of LMMO were determined to be $a = 4.9367(1)$ Å, $b = 8.5951(3)$ Å, $c = 5.0266(1)$ Å, and $\beta = 109.084(3)$ of the C 1 2/m 1 (monoclinic, #12) space group. The values differed by less than 0.8% from the lattice parameters of LMO (Figure S3, Supporting Information), proving that the Mg substitution does not alter the crystal structure. Tables S1 and S2 (Supporting Information) provide detailed structural information for LMMO and LMO, including the atomic position, thermal factor, and occupancy. As shown in Table S3 (Supporting Information), the results confirmed that all Mg cations exist in Mn1 and Li1 sites in the transition metal (TM) layers. In the case of Li2 and Li3 sites in the Li layers, the occupancies of the Mg element were negligible. The low values of the reliability factor ($R_P = 2.46\%$, $R_I = 3.24\%$, $R_F = 6.31\%$, and $\chi^2 = 1.78\%$) confirm the high accuracy of the Rietveld refinement. The X-ray absorption nearest edge spectroscopy (XANES, Mn K-edge) analysis revealed the tetravalent oxidation state of Mn in LMMO, identical to that in LMO (Figure S4, Supporting Information). The TEM–EDS mapping of LMMO results indicate the uniform distribution of Mg, Mn, and O throughout the particles without local irregularity (Figure 1c). In addition, scanning electron microscopy (SEM) analyses show the average particle
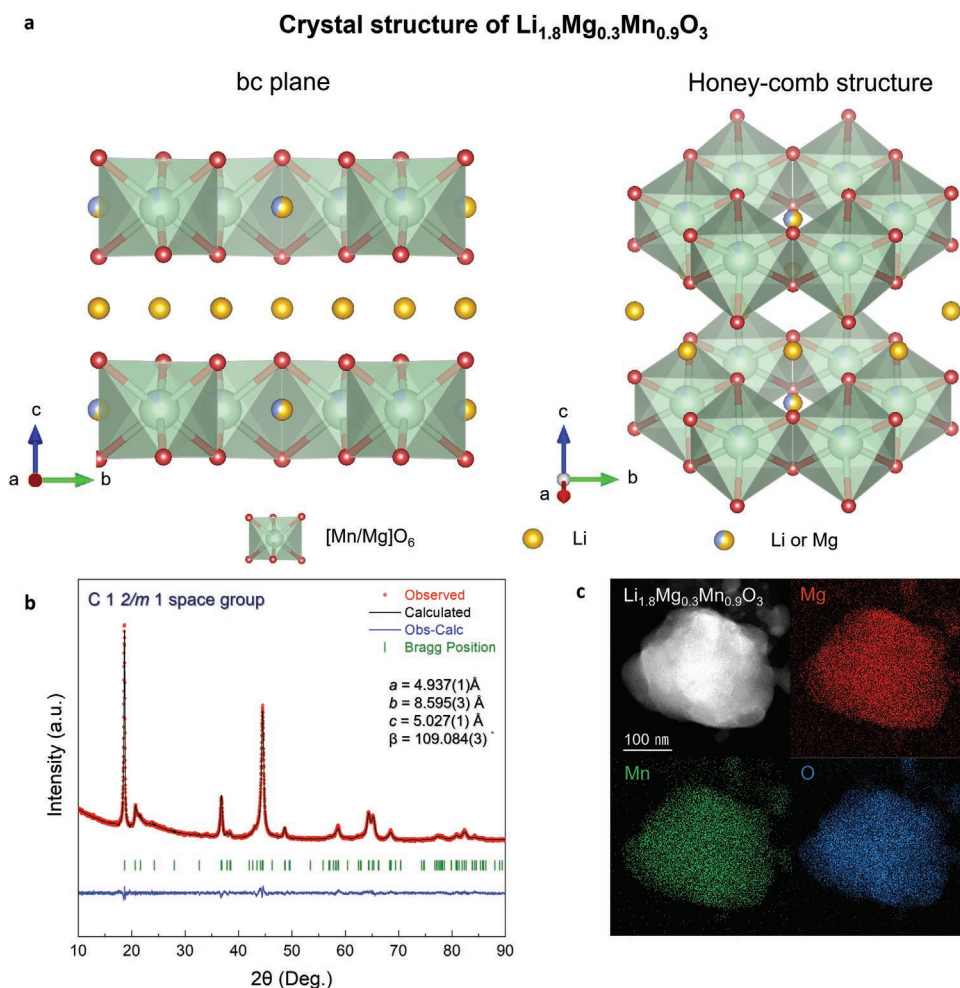
Figure 1. a) Crystal structures, b) Rietveld refinement of XRD pattern of $Li_{1.8}Mg_{0.3}Mn_{0.9}O_3$ considering the Mg occupancy at Li site ($R_P = 2.46\%$, $R_I = 3.24\%$, $R_F = 6.31\%$, and $\chi^2 = 1.78\%$) and c) TEM images with EDS mapping of $Li_{1.8}Mg_{0.3}Mn_{0.9}O_3$.

sizes of LMMO and LMO particles were ≈300 nm, and both samples exhibit the similar morphologies (Figure S5, Supporting Information).

2.2. Electrochemistry of Li1.8Mg0.3Mn0.9O3 (LMMO) in LIB System

To confirm the effect of Mg substitution in the structure, we evaluated various electrochemical properties of LMMO and LMO in the voltage range of 4.8–1.5 V (vs Li/Li+). **Figure 2**a,b shows that LMMO exhibited a large initial discharge capacity of ≈310 mAh g^{-1} with a high initial CE of ≈95.4% at a current density of 30 mA g^{-1}, whereas the initial discharge capacity of LMO was only ≈261 mAh g^{-1} with a relatively poor initial CE of ≈85.3% under the same conditions. Furthermore, LMMO retained up to ≈72% of the initial specific capacity with a high CE of above 99% for 200 cycles at 1 A g^{-1} after the pre-cycle at 30 mA g^{-1}, whereas LMO only exhibited capacity retention of ≈44% with relatively poor CE under the same conditions (Figure 2c; Figure S6, Supporting Information). We attribute the capacity fading of $Li_{1.8}Mg_{0.3}Mn_{0.9}O_3$ to the side reactions

such as electrolyte decomposition during the high-voltage charging process, which is essential for the activation of the anionic redox reaction.[36–38]

Therefore, we supposed that the cycle performance can be degraded after several hundred cycles despite the well retained crystal structure and morphology of the cathode materials.

In addition, to further demonstrate the feasibility of adopting LMMO in practical LIBs, we tested and compared the cycle performances of the LMMO- and LMO-based full cells with a graphite anode in the LIB system for 200 cycles at 1 A g^{-1} after pre-cycle at 30 mA g^{-1} (Figure S7, Supporting Information). In the voltage range of 4.7–1.4 V at 1 A g^{-1}, the LMMO‖graphite full cell delivered a large initial capacity of ≈223 mAh g^{-1} and capacity retention of ≈`70% for 200 cycles. However, the LMO‖graphite full cell only exhibited a small initial capacity of 127 mAh g^{-1}, and its specific capacity was only maintained to ≈25% of the initial capacity under the same conditions. These results indicate that LMMO can deliver more stable electrochemical behavior and anionic redox reaction than LMO, owing to the presence of Mg^{2+} in the structure.

In addition to capacity retention, another challenge for the practical application of Li-rich layered oxide materials is
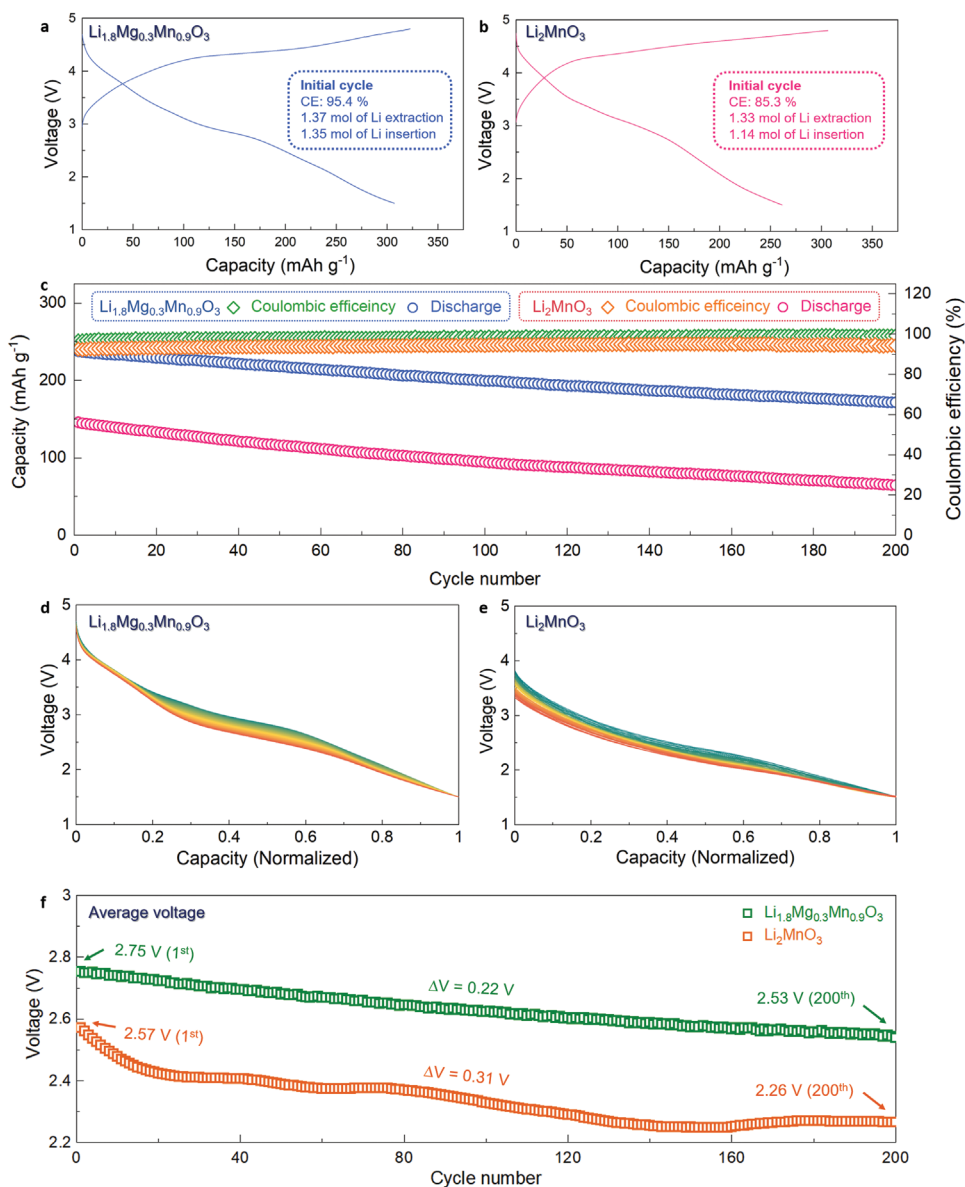
**ADVANCED
SCIENCE NEWS**

www.advancedsciencenews.com

**ADVANCED
FUNCTIONAL
MATERIALS**

www.afm-journal.de

Figure 2. Charge/discharge curves for initial cycle of a) $Li_{1.8}Mg_{0.3}Mn_{0.9}O_3$ and b) Li_2MnO_3 at 30 mA g^{-1}. Comparison of c) cycle performances, d,e) normalized discharge curves and f) average discharge voltages for 200 cycles at 1 A g^{-1} between $Li_{1.8}Mg_{0.3}Mn_{0.9}O_3$ and Li_2MnO_3.

mitigation of the long-term voltage fade to consistently deliver high energy. The normalized discharge profiles (Figure 2d,e) and the differential capacity versus voltage curves (Figure S8, Supporting Information) show the sharp contrast between the electrochemistry of LMMO and LMO. Although the cathodic reaction of LMMO remains active after 200 cycles, LMO loses the faradaic reactions after 100 cycles. The quantitative comparison of the average discharge voltage in Figure 2f reveals ≈8% (220 mV) and ≈12% (310 mV) voltage decreases for LMMO and LMO, respectively, after 200 cycles. The synergetic effect of better capacity retention and voltage retention of LMMO results in the ≈314% higher energy density available after 200 cycles relative to that of LMO (Figure S9, Supporting Information).

Through XRD analysis of the 200-cycled electrodes (Figure S10, Supporting Information), we demonstrated that the original crystal structure of LMMO was well retained without considerable degradation during prolonged cycling. The high structural stability of the Mg-substituted LMMO is attributable to the stable electrochemical behavior. In contrast, the XRD patterns of LMO significantly changed. The superstructure peaks, i.e., in-plane ordering, disappeared; the intensity of the (001) peak significantly decreased; and new diffraction peaks appeared at 42°–43°, suggesting severe structural disordering and phase transformation after the repeated charge/discharge. These results indicate that Mg substitution effectively suppresses the structural disordering while enabling a high practical capacity and voltage.

2.3. Suppressed Structural Evolution in $Li_{1.8}Mg_{0.3}Mn_{0.9}O_3$ (LMMO)

To verify the beneficial effect of Mg^{2+} cations improving the structural stability, we investigated the structural evolution of LMMO and LMO during the initial electrochemical cycling using structural probes, including high-angle annular dark-field scanning transmission electron microscopy (HAADF-STEM), selected area electron diffraction (SAED), and operando and ex-situ XRD. The HAADF-STEM images in **Figure 3**a–d and Figure S11 (Supporting Information) indicate that LMMO maintained the typical layered structure before and after the initial cycle, without a trace of Mn/Mg migration into the Li layers. It is worth highlighting that LMMO does not suffer from Mn/Mg migration into the Li layers while exhibiting a high reversible capacity of 310 mAh g^{-1}, utilizing 75% of the total

Li$^+$ in the active material. In contrast, changes in the atomic arrangement and formation of rock-salt or spinel-like disordered phases by cation-mixing were observed in LMO after the initial cycle. A significant number of heavy atoms, such as Mn, migrated into Li layers, likely occupying the Li octahedral sites.

Operando and ex-situ XRD analyses (Figure 3e,f; Figure S12, Supporting Information) confirm that the observed changes of the overall crystallographic structures were consistent with the HAADF-STEM results. Both the (001) peaks at 18° of LMMO and LMO shifted toward high 2θ angles during Li$^+$ deintercalation and recovered to the near-original position after Li$^+$ reintercalation. These results indicate the reversible shrinkage and expansion of the c-lattice parameters during Li$^+$ de/intercalation (Figure 3g,h). At the same time, the peak width and intensity varied. However, the 2θ degree of change in LMMO was much lower than that in LMO. For LMO, a new peak
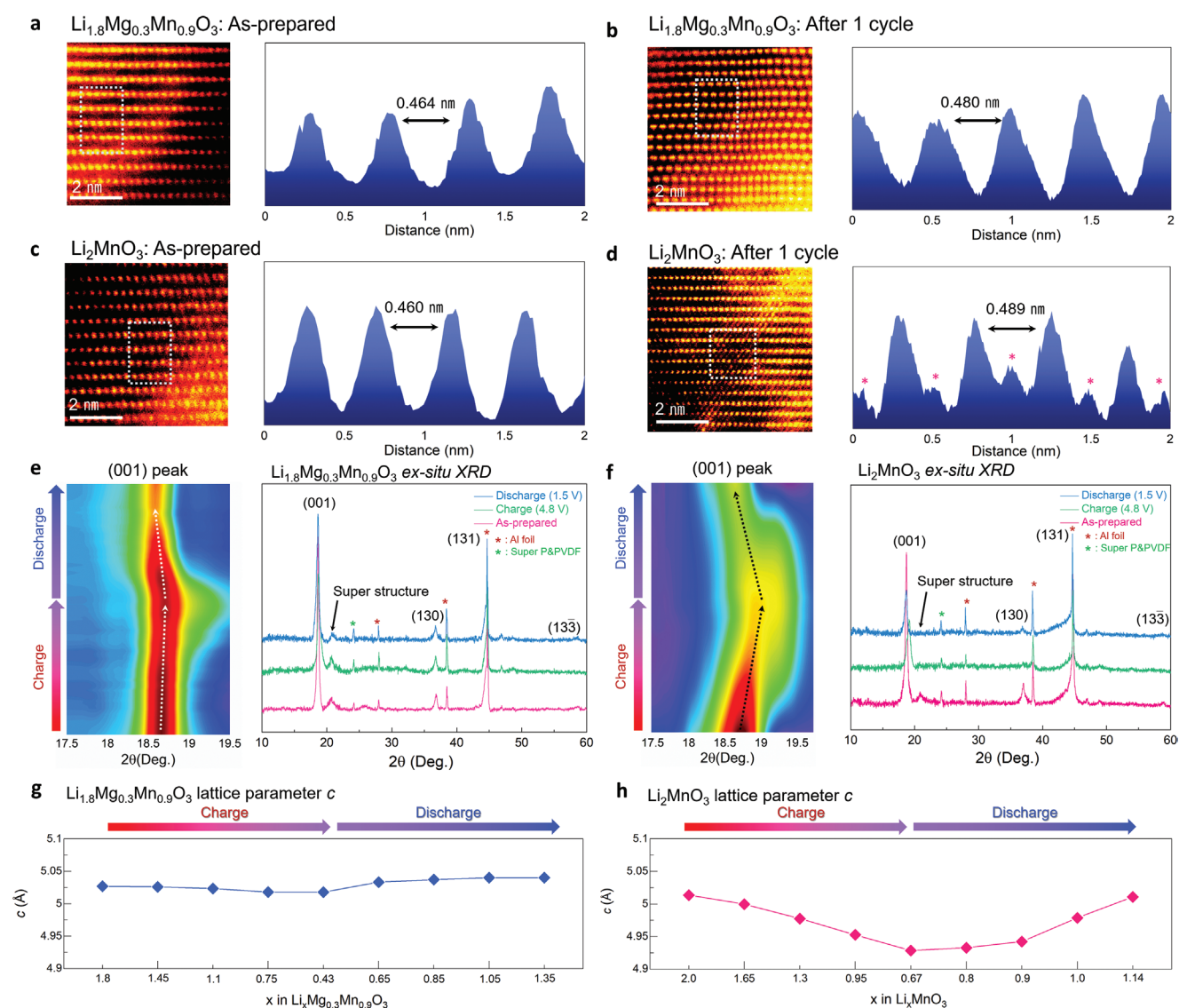

Figure 3. HAADF-STEM images and signal profile of marked region of a) as-prepared $Li_{1.8}Mg_{0.3}Mn_{0.9}O_3$, b) $Li_{1.8}Mg_{0.3}Mn_{0.9}O_3$ after 1 cycle, c) as-prepared Li_2MnO_3, and d) Li_2MnO_3 after 1 cycle. Operando/ex situ XRD patterns of e) $Li_{1.8}Mg_{0.3}Mn_{0.9}O_3$ and f) Li_2MnO_3 during charge/discharge. The change in lattice parameter c of g) $Li_{1.8}Mg_{0.3}Mn_{0.9}O_3$ and h) Li_2MnO_3 as a function of Li content.

**ADVANCED
SCIENCE NEWS**
www.advancedsciencenews.com

**ADVANCED
FUNCTIONAL
MATERIALS**
www.afm-journal.de

appeared at 19° (Figure S13, Supporting Information), and the superlattice peaks at 20°–22° completely disappeared in the XRD pattern after Li$^+$ deintercalation. After Li$^+$ re-intercalation, the intensity of the (001) peak decreased, and a broad feature arose at 40°–43°. All these observations indicate that LMO suffered from severe phase transformation and structural disordering during charge/discharge, losing the layered structure.[16,39] In contrast, the intensities of the (001) peak and superlattice peaks of LMMO were maintained throughout the initial cycle, demonstrating the superior structural stability of LMMO. Furthermore, the change of the c-lattice parameter in LMMO was only ≈0.46% of the slab distance, whereas that in LMO was ≈1.67% of the slab distance, revealing the lower chemo-mechanical stress formed in LMMO than in LMO. In addition, Figure S14 and Table S4 (Supporting Information) below show the Rietveld refinement results on the XRD pattern of the 1-cycled Li$_{1.8}$Mg$_{0.3}$Mn$_{0.9}$O$_3$. We verified that Mn elements negligibly exist in all Li sites in the structure, which indicates that Mn-migration to the Li layers hardly occurred in Li$_{1.8}$Mg$_{0.3}$Mn$_{0.9}$O$_3$ after cycling. The multiscale structural probes led us to conclude that the substitution of electrochemically inactive Mg^{2+} plays a vital role in stabilizing the layered structure of the Li-/Mn-rich cathode materials.

The role of Mg^{2+} cations in stabilizing the structure of LMMO was studied using DFT calculations. **Figure 4**a,b showed the changes in the Mn−O and Mg−O bonding distances as a function of the state of charge (SOC) in each material. In the pristine states, the average bonding distances of Mn−O were similar in both materials. Interestingly, we note that three distinct Mn−O bonding natures exist in LMMO (Figure 4c): long Mn−O bonds (1.99–2.03 Å), middle Mn−O bonds (1.92–1.96 Å), and short Mn−O bonds (1.87–1.89 Å). The diverse bonding nature of Mn−O is maintained in the partially and fully delithiated structures of LMMO in the presence of Mg^{2+} with a larger ionic radius (≈0.72 Å) than Mn^{4+} (≈0.53 Å),[40] in contrast to the LMO structure with a uniform Mn−O bonding distance within the wide Li concentration range. This result indicates the heterogeneous oxygen states in LMMO, which can promote the localized anion redox reaction. In contrast, the LMO structure has a uniform Mn−O bonding distance throughout the Li$^+$ deintercalation process.

In the charged states, we observed severe distortion of all the MnO$_6$ octahedra in Li$_1$MnO$_3$. In contrast, in Li$_{0.9}$Mg$_{0.3}$Mn$_{0.9}$O$_3$, the changes in the MnO$_6$ shape were alleviated by the neighboring MgO$_6$ octahedra (Figure S15, Supporting Information). Instead, the distance between O and redox-inactive Mg^{2+} became heterogeneous. The lengths of the Mg−O bonds were 2.04–2.06 Å in the pristine LMMO state. The Li$^+$ deintercalated LMMO possessed long Mg−O bonds (2.09–2.16 Å), moderate Mg−O bonds (2.03–2.05 Å), and short Mg−O bonds (1.98–1.99 Å). The particularly short bonding indicates that the anionic redox reaction occurred locally on the specific oxygen anions, possibly forming Mg=O double bonds. We believe that the intrinsically heterogeneous local structures, resulting localized anion redox, and presence of Mg^{2+} possibly stabilize the lattice structure without further severe distortions during Li$^+$ de/intercalation. Consequently, the volume of MnO$_6$ octahedral sites remains larger in LMMO than LMO on average during Li$^+$ de/intercalation (Figure 4d), which might be related to the high structural stability of LMMO.

To determine the origin of the improved structural stability achieved with the introduction of Mg^{2+} cations, we compared the thermodynamic stability of the migration of Mn cations to the Li layers in the Li$^+$-deintercalated Li$_0$Mg$_{0.3}$Mn$_{0.9}$O$_3$ and Li$_0$MnO$_3$ structures. **Figure 5**a shows the intermediate and final states of Mn migration in Li$_0$Mg$_{0.3}$Mn$_{0.9}$O$_3$ and Li$_0$MnO$_3$. The Mn migrates from the octahedral site in the TM layer to the Li layer via the adjacent tetrahedral site. Interestingly, the Mn migration in Li$_0$Mg$_{0.3}$Mn$_{0.9}$O$_3$ is energetically unfavorable, even to the neighboring tetrahedral sites (Figure 5b), and the Mn migration and structural disordering in Li$_0$MnO$_3$ are thermodynamically favorable, consistent with previous reports.[16,20,41,42]

Moreover, we observed a significant difference between the Li$_0$MnO$_3$ structures before and after the Mn migration (Figure 5c). The Mn migration in Li$_0$MnO$_3$ induces the deco-ordination of Mn−O bonding, which can effectively stabilize the structure with the oxidized oxygen anions. As a result, severe distortion of MnO$_6$ octahedra near the vacancy (V_{Mn}) occurs, eventually forming the O−O dimers with a bond distance of ≈1.39 Å. The disordering-driven oxygen dimerization likely promotes the formation of molecular oxygen, resulting in deterioration of the electrochemical performance.[43,44] However, in the Li$_0$Mg$_{0.3}$Mn$_{0.9}$O$_3$ structure, the oxidized oxygen species can stably exist without severe structural distortion while maintaining the bond with Mg remaining in the TM layer (Figure 5d). We speculate that the structural stabilization achieved by Mg^{2+} in Li$_0$Mg$_{0.3}$Mn$_{0.9}$O$_3$ can be attributed to the absence of the orbital hybridization between Mg and O, the rigidity of the MgO$_6$ octahedra, and the localized oxidation of oxygen species depending on the local environment.[34]

2.4. Stable and Reversible Anionic Redox Reaction of O$^{2−}$/O$^−$ in Li$_{1.8}$Mg$_{0.3}$Mn$_{0.9}$O$_3$ (LMMO)

Further investigation of the electronic structure during Li$^+$ de/intercalation was performed using DFT calculation. To confirm the effect of Mg substitution on the structural stability, the projected density of states (pDOS) of LMMO was calculated using the Heyd–Scuseria–Ernzerhof (HSE06) hybrid functional for more accurate prediction of the anionic redox reaction.[45] **Figure 6**a shows the pDOS of Mn 3d and O 2p in the Li$_x$Mg$_{0.3}$Mn$_{0.9}$O$_3$ (x = 1.8, 0.9, and 0) structure. The dominant electron density in O 2p near the Fermi level indicates that Li$^+$ can be deintercalated in the Li$_x$Mg$_{0.3}$Mn$_{0.9}$O$_3$ structure through the oxygen redox reaction. As expected, the electron density in O 2p near the Fermi level was changed to the hole density in O 2p, as Li$^+$ was completely deintercalated from the structure, confirming the occurrence of the anionic redox reaction at LMMO. Further analyses of the electronic structure were performed by visualizing the electron and hole densities of Li$_x$Mg$_{0.3}$Mn$_{0.9}$O$_3$. As illustrated in Figure 6b, the electron density was observed at whole Mn and O atoms in the Li$_{0.9}$Mg$_{0.3}$Mn$_{0.9}$O$_3$ structure. During the delithiation process, the hole density of Li$_{0.9}$Mg$_{0.3}$Mn$_{0.9}$O$_3$ was partially generated, and the hole density of O in the dashed line explosively increased in Li$_0$Mg$_{0.3}$Mn$_{0.9}$O$_3$. It was thought that oxygen present in local environments close to Mg would trigger these selective redox reactions in LMMO, whereas all the O elements in the LMO
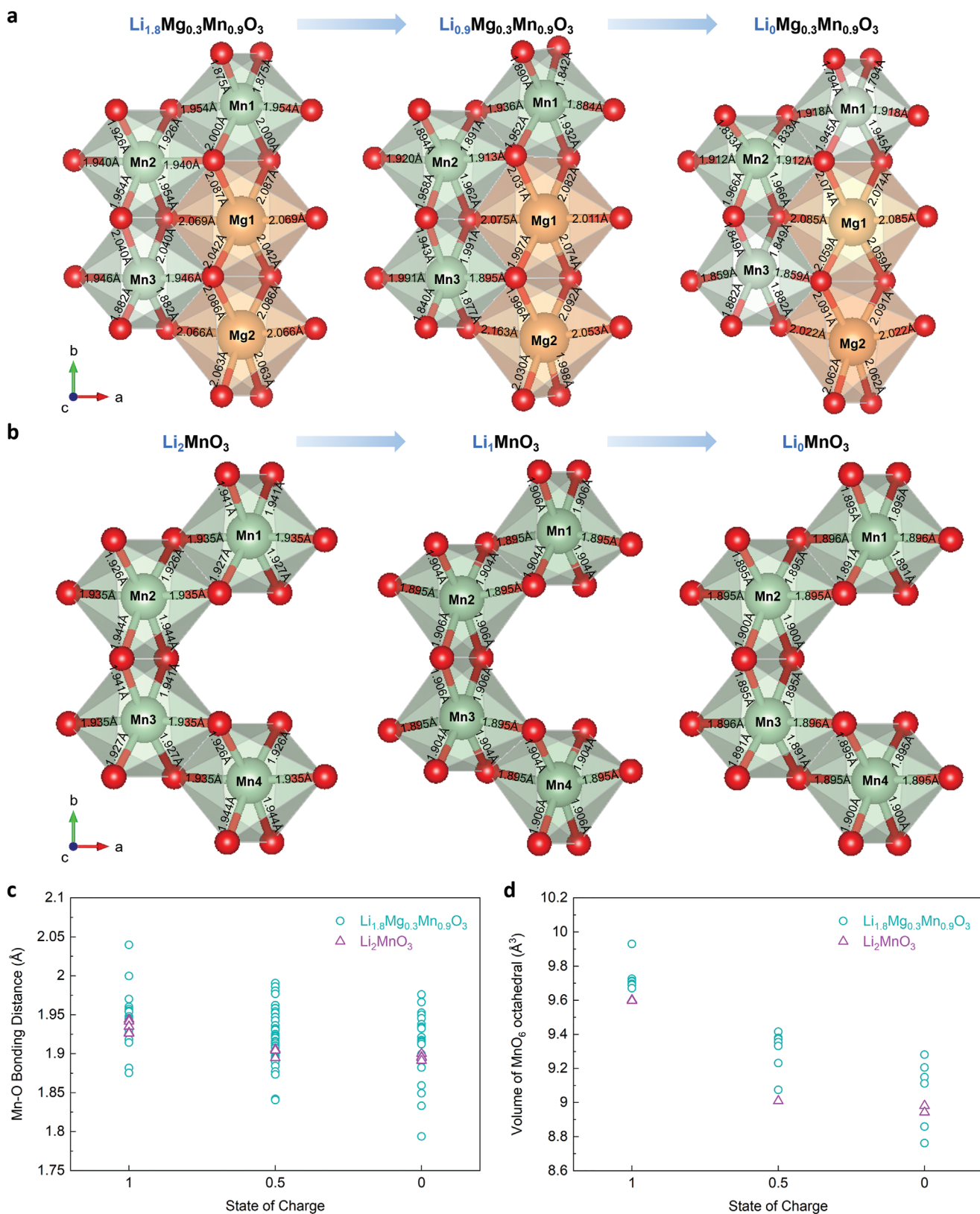
Figure 4. Comparison of Mn−O and Mg−O bonding distances for a) $Li_{1.8}Mg_{0.3}Mn_{0.9}O_3$ and b) Li_2MnO_3 according to the state of charge. Changes in c) total bonding distances of Mn−O and d) total volume of MnO_6 octahedral in $Li_{1.8}Mg_{0.3}Mn_{0.9}O_3$ and Li_2MnO_3 according to the state of charge (SOC).

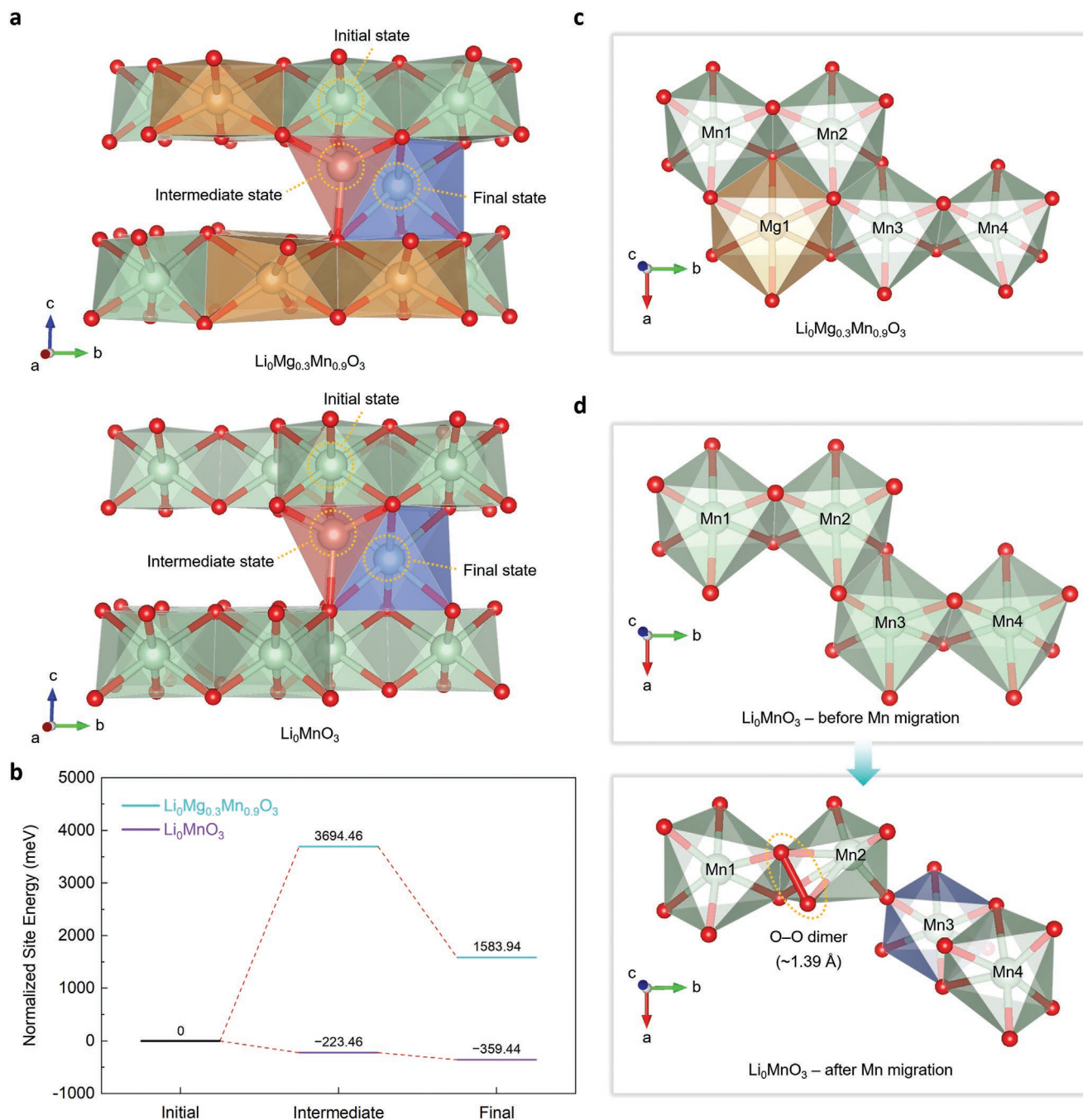**Figure 5.** a) Illustration of Mn migration pathways of $Li_0Mg_{0.3}Mn_{0.9}O_3$ and Li_0MnO_3. b) Comparison of site energies for intermediate state (tetrahedra site) and final state (octahedra site in Li layer) calculated along the Mn migration pathway. Magnified view of crystal structures in c) $Li_0Mg_{0.3}Mn_{0.9}O_3$ and d) Li_0MnO_3 before and after Mn migration.

structure exhibited a similar shape of hole density (Figure S16, Supporting Information). In addition, changes in the effective charges of LMMO and LMO were identified through Bader charge analysis (Figure S17, Supporting Information). It was confirmed that the effective charge of Mn cations does not change significantly in the entire composition range, whereas the O element provides electrons according to Li^+ deintercalation. These results indicate the occurrence of the oxygen redox reaction (O^{2-}/O^-) for Li^+ de/intercalation at LMMO and LMO.

In particular, it was confirmed that the selective oxygen redox reaction occurred in the LMMO structure, whereas uniform charge transfer occurred in the LMO structure (Table S5, Supporting Information).

The cation and anion oxidation behaviors of LMMO and LMO were analyzed using ex situ X-ray absorption near-edge structure (XANES) and extended X-ray absorption fine structure (EXAFS) measurements. In both of the Mn K-edge XANES spectra, the oxidization to Mn^{5+} was not observed during the
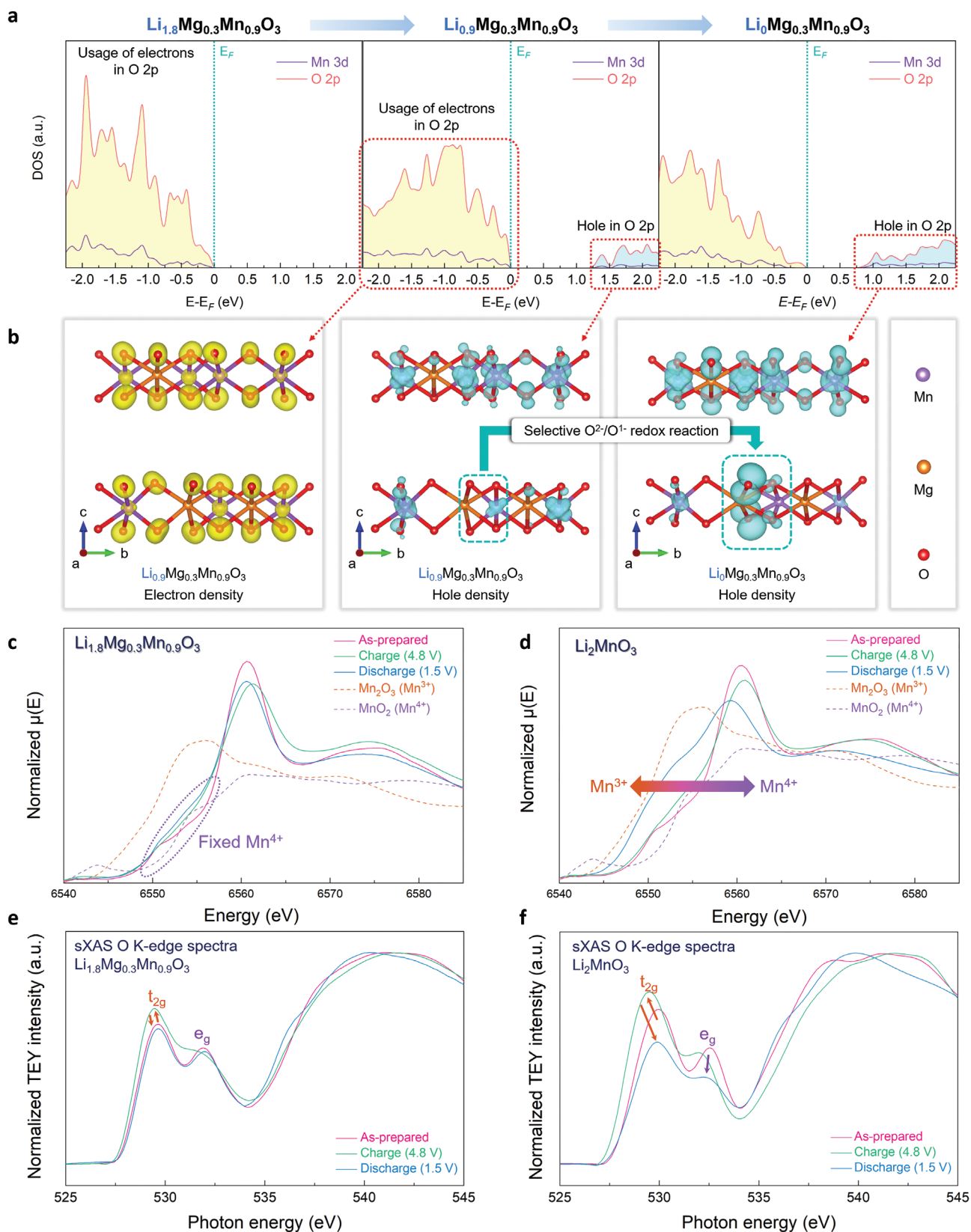
Figure 6. a) Projected density of states of O 2p orbitals of $Li_xMg_{0.3}Mn_{0.9}O_3$ ($x = 1.8$, 0.9, and 0). b) Visualized electron density (yellow) and hole density (blue) for Mn 3p and O 2p orbitals on $Li_{0.9}Mg_{0.3}Mn_{0.9}O_3$ and $Li_0Mg_{0.3}Mn_{0.9}O_3$. Ex situ Mn K-edge XANES spectra of c) $Li_{1.8}Mg_{0.3}Mn_{0.9}O_3$ and d) Li_2MnO_3. Ex situ O K-edge sXAS spectra in TEY mode of e) $Li_{1.8}Mg_{0.3}Mn_{0.9}O_3$ and f) Li_2MnO_3.

charge process, in comparison with the MnO_2 (Mn^{4+}) spectra (Figure 6c,d). In addition, they shifted toward lower (higher) energy level in the charge (discharge) process, indicating the change of the local environment of Mn ions in the structure.[46–48] This finding implied that the additional capacity was attributed to the anionic redox reaction of oxygen ions. For LMMO, negligible change occurred in the oxidation number of Mn during the entire charge/discharge process; thus, distortion of the MnO_6 octahedra in the LMMO structure was considered to be effectively suppressed by the presence of Mg^{2+} cations. However, the Mn K-edge spectra of the LMO drastically shifted close to the trivalent state (Mn^{3+}) in the charge process, which results from the distorted coordination change of the local Mn environment in the LMO structure by oxygen loss or structural disordering occurring during Li^+ de/intercalation. These XANES results on the difference of the local structural change between LMMO and LMO were also confirmed through the Fourier-transform EXAFS analyses (Figure S18, Supporting Information). Although both of peaks for the as-prepared LMMO and LMO had similar intensities, there was a noticeable difference after charge/discharge. The rates of intensity decrease from the as-prepared to charged samples of LMMO were ≈88% (Mn–O) and ≈101% (Mn–Mn), whereas those of LMO were only ≈77% (Mn–O) and ≈71% (Mn–Mn). Even though the peak intensities of not only LMMO but also LMO slightly returned after discharge, the peak intensity in the discharged LMMO state was much more similar to that of the as-prepared peak than to that of the discharged LMO state. The intensity decrease originates from oxygen loss or structure disorder in the octahedral MnO_6 environment.[15,48,49] Although the removal of Li^+ from the lattice affects the bond strain between neighboring atoms, it was considered that substituted Mg^{2+} cations may help to maintain the structure stably. Therefore, we speculate that Mg^{2+} cations enable good retention of the cation ordering in the TM layers of LMMO and suppress the distorted coordination change in the local Mn environment.

In addition, we compared the participation of oxygen anions in charge compensation of LMMO and LMO in (Figure 6e,f) using O K-edge soft X-ray absorption spectroscopy (sXAS) measured in total electron yield (TEY) mode. The pre-edge peaks (at around 530 eV) of O K-edge correspond to metal 3d states, specifically the states of Mn 3d-O 2p orbitals to t_{2g} and e_g hybrid molecular orbitals. In LMMO, the intensity of oxygen pre-edge peaks increase, especially at 529.6 and 531.5 eV during charge, indicating the creation of hole state at the Mn 3d-O 2p level. After discharge, the spectra recovered the original shape of the as-prepared state. In contrast, the O K-edge spectra of LMO undergo significant evolution during cycling, attributable to the irreversible atomic rearrangement triggered by oxygen release. The results point to the fact that Mg substitution in LMMO enabled the highly reversible oxygen redox reaction with negligible O_2 loss, which is fundamentally different from those typically observed in many Li-excess materials. We believe the high reversibility of oxygen redox offers LMMO excellent electrochemical performances with long-term stability. Moreover, to quantify the gas emissions, in situ differential electrochemical mass spectrometry (DEMS) analyses were performed to compare LMMO and LMO during the electrochemical experiments (Figure S19, Supporting Information). A large amount of CO_2 evolution was observed during the initial charge of both samples, which is strongly related to the electrolyte decomposition.[48,50] Interestingly, LMMO exhibited much lower O_2 emission compared with LMO, indicating an improvement in the structural stability through Mg substitution. In the low-voltage region, during the discharge process, electrolyte decomposition and irreversible structural changes did not occur; thus, the gas emission of both samples was significantly reduced. Based on the combined studies with first-principles calculation and various analyses, we confirmed that Mg substitution is helpful for structural change as well as overall crystallinity improvement.

2.5. $Li_{1.8}Mg_{0.3}Mn_{0.9}O_3$ (LMMO) as the Low-Cost and High Energy Cathode for LIBs

We performed additional electrochemical tests to compare the power capability and energy densities of LMMO and LMO. The electrochemical properties were measured in the voltage range of 1.5–4.8 V (vs Li^+/Li) after a pre-cycle at 30 mA g^{-1} and a charge current density of 30 mA g^{-1}. As shown in **Figure 7**a,b, the specific capacity and energy density of LMMO at 30 mA g^{-1} were ≈310 mAh g^{-1} and ≈915 Wh kg^{-1}, respectively, which are larger than those of LMO measured under the same conditions (≈264 mAh g^{-1} and ≈739 Wh kg^{-1}). In particular, in terms of LMMO, even at 1500 mA g^{-1}, its capacity was maintained up to the specific capacity of ≈226 mAh g^{-1}, corresponding to ≈73% of the capacity measured at 30 mA g^{-1}. However, the capacity of LMO at 1500 mA g^{-1} was only ≈103 mAh g^{-1}, which is ≈44% of the capacity at 30 mA g^{-1} (Figure 7c,d). These results indicate that LMMO exhibits outstanding power capability as a promising cathode for low-cost and high-energy LIBs, unlike LMO. Furthermore, to confirm that LMMO can be applied as a cathode in practical LIB fields, we compared the electrochemical properties of LMMO with those of several conventional LIB cathode materials, including $LiCoO_2$, $LiNi_{0.8}Co_{0.1}Mn_{0.1}O_2$, $LiNi_{0.8}Co_{0.15}Al_{0.05}O_2$, and $LiNi_{0.6}Co_{0.2}Mn_{0.2}O_2$ (Figure 7e).[30–33] Despite the differences between electrochemical testing conditions, this comparison shows that the novel Mn–Mg layered cathode LMMO can exhibit high competitiveness as one of the promising cathodes for LIBs.

3. Conclusion

In this work, we investigated the novel Li-rich Mn–Mg layered cathode, $Li_{1.8}Mg_{0.3}Mn_{0.9}O_3$ (LMMO) for application in low-cost and high-energy LIBs. Through the presence of redox-inactive Mg^{2+} cations as a structural stabilizer, LMMO exhibits enhanced electrochemical performance compared with Li_2MnO_3 (LMO), which suffers from irreversible structural degradation due to Mn migration to Li layers and the loss of oxygen molecules from the structure. Through DFT calculation, it was revealed that the Mn migration to Li layers in fully Li^+ deintercalated $Li_0Mg_{0.3}Mn_{0.9}O_3$ is thermodynamically unfavorable, unlike that in Li_0MnO_3. In addition, $Li_0Mg_{0.3}Mn_{0.9}O_3$ does not undergo severe distortion of the MnO_6 octahedra and the formation of the O−O dimer related to release of oxygen molecules from the structure. Various structural analyses, including operando XRD
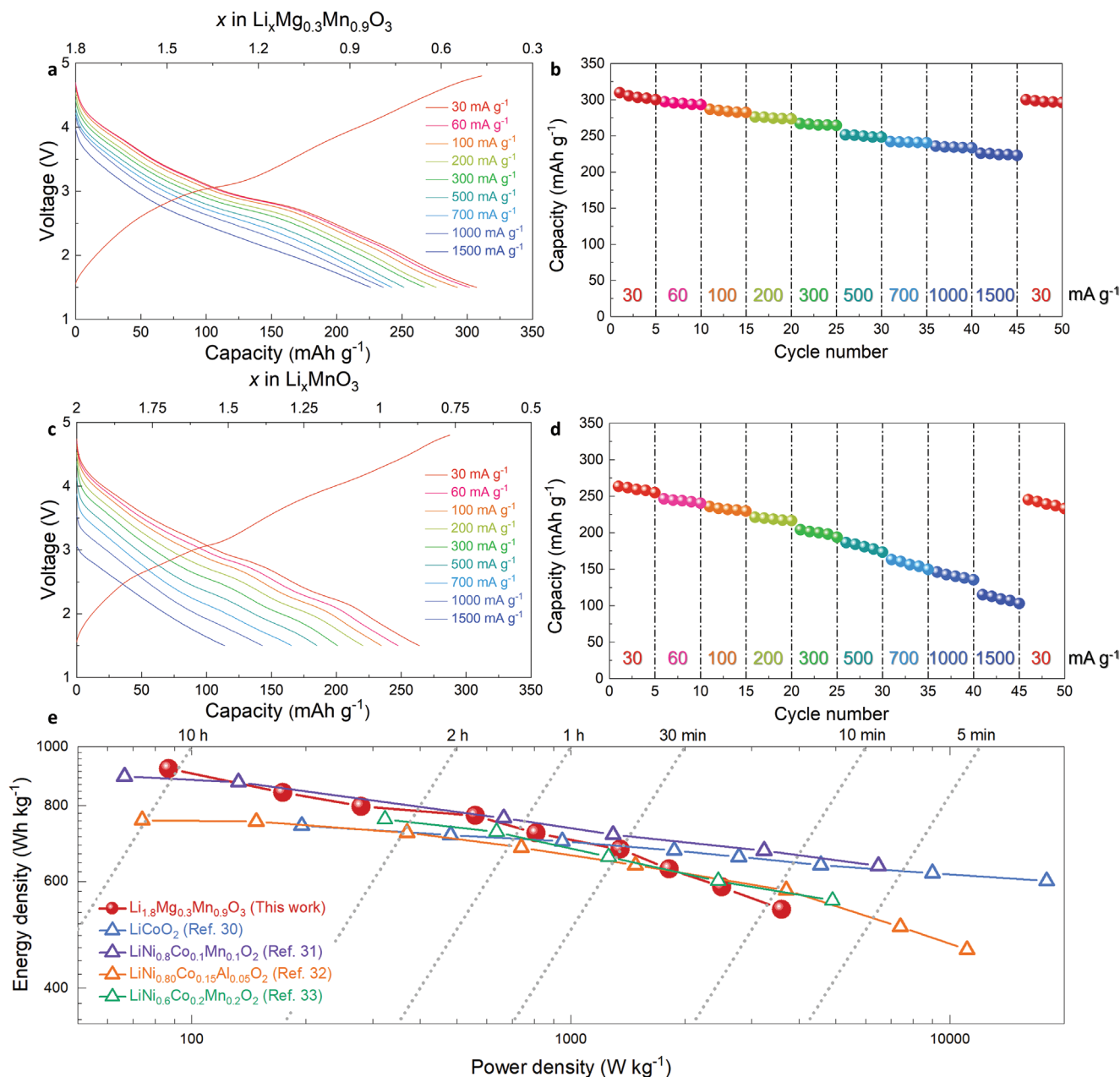
**ADVANCED
SCIENCE NEWS**

www.advancedsciencenews.com

**ADVANCED
FUNCTIONAL
MATERIALS**

www.afm-journal.de

Figure 7. Power capability of a) $Li_{1.8}Mg_{0.3}Mn_{0.9}O_3$ and c) Li_2MnO_3 at various discharge current densities in the voltage range of 1.5–4.8 V and a charge current density of 30 mA g^{-1}. Rate capability of b) $Li_{1.8}Mg_{0.3}Mn_{0.9}O_3$ and d) Li_2MnO_3. e) Ragone plot of $Li_{1.8}Mg_{0.3}Mn_{0.9}O_3$ and other conventional cathode materials for LIBs.

and ex situ XANES, EXAFS, and HADDF-STEM analyses also demonstrated that the irreversible structural disordering was restricted in the LMMO structure during Li$^+$ de/intercalation, compared with the LMO structure. Thus, anionic-redox-based LMMO could deliver distinctly outstanding electrochemical performance compared with LMO, because of the enhanced structural stability by Mg substitution. At 30 mA g^{-1}, the capacity and energy density of LMMO were ≈310 mAh g^{-1} and ≈915 Wh kg^{-1}, respectively, which are larger than those of LMO. Furthermore, we verified that the power-capability and cyclability of LMMO are greatly superior to those of LMO under the same conditions.

The excellent performances promise the utilization of LMMO in Ni-/Co-free next-generation LIBs. Our findings suggest an effective method for overcoming the main issues facing LIBs that should simultaneously result in both an increase of the energy density and reduction of the production cost.

4. Experimental Section

Material Preparation: $Li_{1.8}Mg_{0.3}Mn_{0.9}O_3$ and Li_2MnO_3 were prepared using Li_2CO_3 (Sigma–Aldrich, 99%), MgO (Sigma–Aldrich, 97%), and

$MnCO_3$ (Sigma–Aldrich, 99%) as precursors. The precursors were stoichiometrically mixed using high-energy ball-milling (Taemyong Scientific) at 400 rpm for 12 h in an Ar atmosphere. The mixed powders were then pelletized and calcined at 850 °C for 12 h in air.

Materials Characterization: The crystal structures of $Li_{1.8}Mg_{0.3}Mn_{0.9}O_3$ and Li_2MnO_3 were characterized using X-ray diffraction (XRD, PANalytical) with Cu Kα radiation (wavelength = 1.54178 Å, Bragg–Brentano reflection geometry). The 2θ range was 10°–90° with a time per step of 0.13 s. The FullProf Rietveld program was used to analyze the XRD data.[51] The operando XRD patterns were obtained at the 3D XRS beamline at the Pohang Accelerator Laboratory (PAL) using synchrotron radiation (λ = 0.688725 Å) with a Mar345 image plate detector in transmission mode and an X-ray exposure time of 5 s. After the measurement, the 2θ angles of all the operando XRD patterns were converted into the corresponding angles for λ = 1.54178 Å (the wavelength of a conventional X-ray tube source with Cu Kα radiation) for ease of comparison with other studies.

The morphology of the materials was examined using field-emission scanning electron microscopy (FE-SEM; SU-8010). Energy-dispersive X-ray spectroscopy (EDS) elemental mapping was performed using high-resolution transmission electron microscopy (HR-TEM; JEM-3010) at the National Center for Inter-university Research Facilities (NCIRF) at Seoul National University. HR-TEM particle images and atomic-resolution high-angle annular dark field-scanning transmission electron microscopy (HAADF-STEM) images were obtained using a Cs-corrected microscope (FEI, TITAN TM 80–300) operated at 300 keV.

Ex situ X-ray absorption spectroscopy (XAS) spectra for the Mn K-edge were obtained at the 10 C Wide XAFS beamline at PAL. Mn K-edge spectra were collected in transmission mode with an energy range of 6540–6585 eV, including the X-ray absorption near-edge structure (XANES) and extended X-ray absorption fine structure (EXAFS) regions, and Mn reference spectra were simultaneously obtained from Mn metal foil. Soft X-ray absorption spectroscopy (sXAS) spectra for the O K-edge were measured in high-energy grating (HEG) with a photon energy range of 525–560 eV at the 4D PES beamline at PAL. The collected XAS and sXAS data were analyzed using Athena software.[52]

Electrochemical Characterization: The active materials were mixed with conductive carbon (active material:Super P:carbon nanotubes (CNTs) = 80:19:1 by weight) using high-energy ball-milling at 300 rpm for 12 h. The $Li_{1.8}Mg_{0.3}Mn_{0.9}O_3$ and Li_2MnO_3 electrodes were prepared by mixing the active material, Super P as the conducting carbon, and poly(vinylidene fluoride) (PVDF) as the binder using *N*-methyl-2-pyrrolidone (NMP) as the solvent. A slurry (87.5 wt.% active material, 2.5 wt.% Super P, and 10 wt.% PVDF) was applied to Al foil using a doctor blade. The electrodes consisted of 70 wt.% $Li_{1.8}Mg_{0.3}Mn_{0.9}O_3$ or Li_2MnO_3 as the active material, 20 wt.% conductive carbon, and 10 wt.% PVDF binder. Each electrode was dried in a vacuum oven at 80 °C for 12 h to evaporate the NMP. The mass loading of the electrode was ≈2 mg cm^{-2}. Coin cells (2032-type) were prepared using the $Li_{1.8}Mg_{0.3}Mn_{0.9}O_3$ / Li_2MnO_3 electrode, Li metal as the reference/counter electrode, a separator (Celgard 2400), and 1.0 M $LiPF_6$ in EC:DMC (volume ratio of 3:7) as the electrolyte. The coin cells were assembled in an Ar-filled glove box. Galvanostatic charge/discharge tests were performed at various current rates (300–1500 mA g^{-1}) in the voltage range of 1.5–4.8 V (vs Li$^+$/Li) using a battery test system (WonATech WBCS3000).

Full cells were assembled using commercial graphite (Sigma–Aldrich, powder, >20 µm) as the anode material. The graphite electrode was fabricated using the same procedure and ratio as the $Li_{1.8}Mg_{0.3}Mn_{0.9}O_3$ / Li_2MnO_3 electrode, except for the use of Cu foil. To minimize the irreversibility of graphite, the graphite electrode was pre-cycled by direct contact with Li metal in 1.0 M $LiPF_6$ in EC:DMC (volume ratio of 3:7) electrolyte. Finally, R2032-type full cells were assembled with the $Li_{1.8}Mg_{0.3}Mn_{0.9}O_3$ / Li_2MnO_3 electrode and pre-cycled graphite electrode (capacity ratio of negative and positive electrodes of ≈1.2) in an Ar-filled glove box.

In situ differential electrochemical mass spectrometry (DEMS) analysis was performed using the mass spectroscopy (Hiden Analytical,

UK) to compare the amount of O_2 and CO_2 gases generated during charge. The $Li_{1.8}Mg_{0.3}Mn_{0.9}O_3/Li_2MnO_3$ cells were continuously purged with Ar gas, which carried the emitted gas to the mass spectrometer for MS analyses, and connected to the DEMS analysis line. The cells were charged/discharged at a current density of 30 mA g^{-1} in the voltage range of 1.5–4.8 V and changes in ion current were monitored as a function of time.

Computational Details: All the DFT calculations were performed using the Vienna Ab initio Simulation Package (VASP).[53] Projector-augmented wave (PAW) pseudopotentials[54] with a plane-wave basis set, as implemented in VASP were used. Perdew–Burke–Ernzerhof (PBE) parametrization of the generalized gradient approximation (GGA)[55] was used for the exchange-correlation functional. For the DFT calculations, a $6 \times 3 \times 3$ k-point grid was used to calculate a $1 \times 1 \times 2$ supercell structure of $Li_{14}Mg_3Mn_7O_{24}$ and $Li_{16}Mn_8O_{24}$. The GGA+U method[56] was adopted to address the localization of the *d*-orbital in Mn ions, with a U value of 3.9 eV, as determined in a previous report.[9,57] The Heyd–Scuseria–Ernzerhof (HSE06) hybrid functional[43] was applied to accurately calculate the projected density of states (pDOS) of Mn and O.[9,58] A kinetic-energy cutoff of 500 eV was used in all the calculations, and all the structures were optimized until the force in the unit cell converged to within 0.03 eV Å^{-1}.

Cluster-assisted statistical mechanics (CASM)[59] software was used to generate all the Li/vacancy configurations for each composition, followed by performing DFT calculations on a maximum of twenty configurations with the lowest electrostatic energy for each composition used to obtain the convex hull of the $Li_{14}Mg_3Mn_7O_{24}$ and $Li_{16}Mn_8O_{24}$ supercell. Schematic illustrations and the crystal structure were drawn using VESTA software.[60]

Supporting Information

Supporting Information is available from the Wiley Online Library or from the author.

Conflict of Interest

The authors declare no conflict of interest.

Data Availability Statement

The data that support the findings of this study are available from the corresponding author upon reasonable request.

[1] M. Saubanère, E. McCalla, J. M. Tarascon, M. L. Doublet, *Energy Environ. Sci.* **2016**, *9*, 984.

[2] J. B. Goodenough, *Nat. Electron.* **2018**, *1*, 204.

[3] Y. Lyu, X. Wu, K. Wang, Z. Feng, T. Cheng, Y. Liu, M. Wang, R. Chen, L. Xu, J. Zhou, Y. Lu, B. Guo, *Adv. Energy Mater.* **2021**, *11*, 2000982.

[4] N. Nitta, F. Wu, J. T. Lee, G. Yushin, *Mater. Today* **2015**, *18*, 252.

[5] G. Zubi, R. Dufo-López, M. Carvalho, G. Pasaoglu, *Renew. Sustain. Energy Rev.* **2018**, *89*, 292.

[6] London Metal Exchange, https://www.lme.com (accessed Feb 7, **2022**).

[7] E. Cho, K. Kim, C. Jung, S. W. Seo, K. Min, H. S. Lee, G. S. Park, J. Shin, *J. Phys. Chem. C* **2017**, *121*, 21118.

[8] J. Lee, D. A. Kitchaev, D.-H. Kwon, C.-W. Lee, J. K. Papp, Y.-S. Liu, Z. Lun, R. J. Clément, T. Shi, B. D. McCloskey, J. Guo, M. Balasubramanian, G. Ceder, *Nature* **2018**, *556*, 185.

[9] D.-H. Seo, J. Lee, A. Urban, R. Malik, S. Kang, G. Ceder, *Nat. Chem.* **2016**, *8*, 692.

[10] G. Assat, J. M. Tarascon, *Nat. Energy* **2018**, *3*, 373.

[11] S. Zhao, K. Yan, J. Zhang, B. Sun, G. Wang, *Angew. Chem., Int. Ed.* **2021**, *60*, 2208.

[12] D. Y. W. Yu, K. Yanagida, Y. Kato, H. Nakamura, *J. Electrochem. Soc.* **2009**, *156*, A417.

[13] R. Wang, X. He, L. He, F. Wang, R. Xiao, L. Gu, H. Li, L. Chen, *Adv. Energy Mater.* **2013**, *3*, 1358.

[14] P. Yan, L. Xiao, J. Zheng, Y. Zhou, Y. He, X. Zu, S. X. Mao, J. Xiao, F. Gao, J.-G. Zhang, C.-M. Wang, *Chem. Mater.* **2015**, *27*, 975.

[15] R. Kataoka, N. Taguchi, T. Kojima, N. Takeichi, T. Kiyobayashi, *J. Mater. Chem. A* **2019**, *7*, 5381.

[16] K. Shimoda, M. Oishi, T. Matsunaga, M. Murakami, K. Yamanaka, H. Arai, Y. Ukyo, Y. Uchimoto, Y. Ohta, E. Matsubara, Z. Ogumi, *J. Mater. Chem. A* **2017**, *5*, 6695.

[17] H. Chen, M. S. Islam, *Chem. Mater.* **2016**, *28*, 6656.

[18] R. Xiao, H. Li, L. Chen, *Chem. Mater.* **2012**, *24*, 4242.

[19] J. R. Croy, J. S. Park, F. Dogan, C. S. Johnson, B. Key, M. Balasubramanian, *Chem. Mater.* **2014**, *26*, 7091.

[20] K. Nakayama, R. Ishikawa, S. Kobayashi, N. Shibata, Y. Ikuhara, *Nat. Commun.* **2020**, *11*, 4452.

[21] Y. Kan, Y. Hu, C.-K. Lin, Y. Ren, Y.-K. Sun, K. Amine, Z. Chen, *Phys. Chem. Chem. Phys.* **2014**, *16*, 20697.

[22] Y. Sun, H. Cong, L. Zan, Y. Zhang, *ACS Appl. Mater. Interfaces* **2017**, *9*, 38545.

[23] Y. Xiang, X. Wu, *Ionics* **2018**, *24*, 83.

[24] M. Tabuchi, Y. Nabeshima, T. Takeuchi, K. Tatsumi, J. Imaizumi, Y. Nitta, *J. Power Sources* **2010**, *195*, 834.

[25] P. K. Nayak, J. Grinblat, E. Levi, M. Levi, B. Markovsky, D. Aurbach, *Phys. Chem. Chem. Phys.* **2017**, *19*, 6142.

[26] D. Wang, Y. Huang, Z. Huo, L. Chen, *Electrochim. Acta* **2013**, *107*, 461.

[27] H. Li, X. Zhao, Y. Li, Y. Gan, W. Qiu, J. Wang, J. Liu, *J. Mater. Chem. A* **2021**, *9*, 10364.

[28] P. K. Nayak, E. M. Erickson, F. Schipper, T. R. Penki, N. Munichandraiah, P. Adelhelm, H. Sclar, F. Amalraj, B. Markovsky, D. Aurbach, *Adv. Energy Mater.* **2018**, *8*, 1702397.

[29] K. Zhou, Q. Xie, B. Li, A. Manthiram, *Energy Storage Mater.* **2021**, *34*, 229.

[30] X. Li, L. Zhou, H. Wang, D. Meng, G. Qian, Y. Wang, Y. He, Y. Wu, Z. Hong, Z. F. Ma, L. Li, *J. Mater. Chem. A* **2021**, *9*, 19675.

[31] F. Wu, Q. Li, L. Chen, Q. Zhang, Z. Wang, Y. Lu, L. Bao, S. Chen, Y. Su, *ACS Appl. Mater. Interfaces* **2019**, *11*, 36751.

[32] J. Li, M. Liu, J. An, P. Tian, C. Tang, T. Jia, F. K. Butt, D. Yu, W. Bai, C. Cao, X. Feng, *J. Alloys Compd.* **2020**, *829*, 154555.

[33] Y. Chen, S. Tang, S. Deng, T. Lei, Y. Li, W. Li, G. Cao, J. Zhu, J. Zhang, *J. Power Sources* **2019**, *431*, 8.

[34] J. Ahn, J. Kang, M. Cho, H. Park, W. Ko, Y. Lee, H. Kim, Y. H. Jung, T.-Y. Jeon, H. Kim, W.-H. Ryu, J. Hong, J. Kim, *Adv. Energy Mater.* **2021**, *11*, 2102311.

[35] J. Bréger, M. Jiang, N. Dupré, Y. S. Meng, Y. Shao-Horn, G. Ceder, C. P. Grey, *J. Solid State Chem.* **2005**, *178*, 2575.

[36] Y. Zou, Z. Cao, J. Zhang, W. Wahyudi, Y. Wu, G. Liu, Q. Li, H. Cheng, D. Zhang, G. T. Park, L. Cavallo, T. D. Anthopoulos, L. Wang, Y. K. Sun, J. Ming, *Adv. Mater.* **2021**, *33*, 2102964.

[37] K. Guo, S. Qi, H. Wang, J. Huang, M. Wu, Y. Yang, X. Li, Y. Ren, J. Ma, *Small Sci* **2022**, *2*, 2100107.

[38] C. Ye, W. Tu, L. Yin, Q. Zheng, C. Wang, Y. Zhong, Y. Zhang, Q. Huang, K. Xu, W. Li, *J. Mater. Chem. A* **2018**, *6*, 17642.

[39] A. D. Robertson, P. G. Bruce, C. Ye, W. Tu, L. Yin, Q. Zheng, C. Wang, Y. Zhong, Y. Zhang, Q. Huang, K. Xu, W. Li, *J. Mater. Chem. A* **2018**, *6*, 17642.

[40] R. D. Shannon, *Acta Crystallogr., Sect. A: Found. Crystallogr.* **1976**, *32*, 751.

[41] Q. Chen, Y. Pei, H. Chen, Y. Song, L. Zhen, C. Y. Xu, P. Xiao, G. Henkelman, *Nat. Commun.* **2020**, *11*, 3411.

[42] X. Gao, Y. H. Ikuhara, C. A. J. Fisher, R. Huang, A. Kuwabara, H. Moriwake, K. Kohama, Y. Ikuhara, *J. Mater. Chem. A* **2019**, *7*, 8845.

[43] J. Hong, W. E. Gent, P. Xiao, K. Lim, D. H. Seo, J. Wu, P. M. Csernica, C. J. Takacs, D. Nordlund, C. J. Sun, K. H. Stone, D. Passarello, W. Yang, D. Prendergast, G. Ceder, M. F. Toney, W. C. Chueh, *Nat. Mater.* **2019**, *18*, 256.

[44] U. Maitra, R. A. House, J. W. Somerville, N. Tapia-Ruiz, J. G. Lozano, N. Guerrini, R. Hao, K. Luo, L. Jin, M. A. Pérez-Osorio, F. Massel, D. M. Pickup, S. Ramos, X. Lu, D. E. McNally, A. V. Chadwick, F. Giustino, T. Schmitt, L. C. Duda, M. R. Roberts, P. G. Bruce, *Nat. Chem.* **2018**, *10*, 288.

[45] J. Heyd, G. E. Scuseria, *J. Chem. Phys.* **2004**, *121*, 1187.

[46] F. Dogan, J. R. Croy, M. Balasubramanian, M. D. Slater, H. Iddir, C. S. Johnson, J. T. Vaughey, B. Key, *J. Electrochem. Soc.* **2015**, *162*, A235.

[47] K. Luo, M. R. Roberts, N. Guerrini, N. Tapia-Ruiz, R. Hao, F. Massel, D. M. Pickup, S. Ramos, Y.-S. Liu, J. Guo, A. V. Chadwick, L. C. Duda, P. G. Bruce, *J. Am. Chem. Soc.* **2016**, *138*, 11211.

[48] J. Rana, J. K. Papp, Z. Lebens-Higgins, M. Zuba, L. A. Kaufman, A. Goel, R. Schmuch, M. Winter, M. S. Whittingham, W. Yang, B. D. McCloskey, L. F. J. Piper, *ACS Energy Lett.* **2020**, *5*, 634.

[49] C. J. Pelliccione, Y. R. Li, A. C. Marschilok, K. J. Takeuchi, E. S. Takeuchi, *Phys. Chem. Chem. Phys.* **2016**, *18*, 2959.

[50] J. Wu, Z. Cui, J. Wu, Y. Xiang, H. Liu, S. Zheng, W. Yang, Y. Yang, *J. Mater. Chem. A* **2020**, *8*, 18687.

[51] J. Rodríguez-Carvajal, *Comm. Powder Diffr. (IUCr). Newsl.* **2001**, *26*, 12.

[52] B. Ravel, M. Newville, *Phys. Scr.* **2005**, *2005*, 1007.

[53] G. Kresse, J. Furthmüller, *Comput. Mater. Sci.* **1996**, *6*, 15.

[54] P. E. Blöchl, *Phys. Rev. B* **1994**, *50*, 17953.

[55] J. P. Perdew, K. Burke, M. Ernzerhof, *Phys. Rev. Lett.* **1996**, *77*, 3865.

[56] V. I. Anisimov, F. Aryasetiawan, A. I. Lichtenstein, *J. Phys. Condens. Matter* **1997**, *9*, 767.

[57] H. J. Kim, A. Konarov, J. H. Jo, J. U. Choi, K. Ihm, H. Lee, J. Kim, S. Myung, *Adv. Energy Mater.* **2019**, *9*, 1901181.

[58] J. Heyd, G. E. Scuseria, M. Ernzerhof, *J. Chem. Phys.* **2003**, *118*, 8207.

[59] A. Van der Ven, J. C. Thomas, Q. Xu, J. Bhattacharya, *Math. Comput. Simul.* **2010**, *80*, 1393.

[60] K. Momma, F. Izumi, *J. Appl. Crystallogr.* **2008**, *41*, 653.